Editors' Suggestion

Surface exciton formation on InP(110)−(1 × 1) studied by time- and angle-resolved photoemission spectroscopy

Hiroshi Tanimura,[1] Katsumi Tanimura,[2] and Jun'ichi Kanasaki[3]
[1]*Institute for Materials Research, Tohoku University, 2-1-1 Katahira, Sendai 980–8577, Japan*
[2]*The Institute of Scientific and Industrial Research, Osaka University, 8-1 Mihogaoka, Ibaraki, Osaka 567-0047, Japan*
[3]*Department of Mechanical and Physical Engineering, Graduate school of Engineering, Osaka-City University, 3-3-138 Sugimoto, Sumiyoshi, Osaka 565–8585, Japan*

(Received 20 October 2022; revised 4 February 2023; accepted 8 February 2023; published 23 February 2023)

Using time- and angle-resolved photoemission spectroscopy, we study the surface exciton formed on InP(110)-(1 × 1) surface at 90 K under ultrahigh vacuum conditions. The surface exciton shows a characteristic photoemission peak with a long lifetime of 9.5 ns at 90 K. The exciton binding energy is 28 meV, about 5.5 times larger than the energy of bulk excitons. The radial probability density at the lowest state of the exciton is spheroidal, confined within ∼6 Å from the surface along the surface-normal direction with a radial spread of ∼44 Å in the plane parallel to the surface, being a quasi–two-dimensional excitonic state. These features are consistently described in terms of the exciton theory based on the Wannier equation. Both the reduced screening effects and the two-dimensional confinement at the surface region play important roles in charactering the surface exciton on InP(110)-(1 × 1) surfaces.

DOI: 10.1103/PhysRevB.107.075304

I. INTRODUCTION

The surfaces of covalent semiconductors under ultrahigh-vacuum conditions often undergo intrinsic reconstructions/relaxations to minimize the unfavorable energy due to unsaturable bonds, governed by the balance between the energy gained from variations in the bonding properties and the elastic energy lost due to distortions from ideal sp^3 bonding [1–3]. The atomic rearrangements are associated with alteration of the lateral arrangements for several layers parallel to the surface. Therefore, the covalent semiconductor surfaces form quasi–two-dimensional (2D) systems which have atomic and electronic structures significantly different from those of bulk materials, with the unique configurations sandwiched between two boundaries; one is the sharp interface between the surfaces and vacuum and the other is the gradually changing interfaces between the surfaces and bulk materials [1–3].

Because of the continuing miniaturization of semiconductor devices, coupling of bulk electrons to surface and interface states dominates electron dynamics and recombination and ultimately affects device performance [4–7]. Therefore, the electron dynamics on semiconductor surfaces is of both fundamental and technological importance. Among many important issues of surface-carrier dynamics, we focus attention in this paper to one fundamental issue of the surface-specific effects on the characteristics of excitonic states. Excitons are quasiparticles that form when Coulomb-interacting electrons and holes are bound into pair states, and they are intrinsic electronically excited states with the lowest energies in semiconductors in most cases [8–12]. Therefore, the electron-hole correlation, which is the key interaction for exciton formation, plays crucial roles in the dynamics, relaxations, and recombination processes of energetic carriers [13–15].

The excitons formed on the semiconductor surfaces under ultrahigh-vacuum conditions, which provide clean and reproducible surfaces at the nanoscale level [1–3], have been studied based on the microscopic knowledge of the structural, electronic, and optical properties of clean surfaces. Vacuum-cleaved Si(111)-(2 × 1) surfaces show a drastic reconstruction, features of which are well described by the tilted Pandy chain model [1,16–19]. On this surface, a prominent optical absorption band has been detected at 0.43 eV, well below the bulk band-gap energy E_G of Si [20,21]. Theoretical studies using an *ab initio* approach have shown that the surface exciton, composed of a hole in the occupied dangling-bond surface band $D_{\rm up}$ and an electron in the unoccupied dangling-bond band $D_{\rm down}$ of the tilted Pandy chain, is responsible for the strong absorption at 0.43 eV [18,19]. The binding energy E_b of the surface exciton is calculated to be 0.26 eV, more than 18 times larger than that (14.3 meV) of the bulk exciton in Si [10]. On the other hand, the surface exciton on Si(001)-$c(4 \times 2)$ has been studied using time- and angle-resolved photoemission spectroscopy (TR-ARPES) [22,23]. Similar to the case on Si(111)-(2 × 1), the surface exciton is composed of a hole in the occupied dangling-bond surface band $D_{\rm up}$ and an electron in the unoccupied dangling-bond band $D_{\rm down}$ of the tilted Si dimers with $c(4 \times 2)$ stacking. The excitation energy of the surface exciton at the ground state has been determined to be 0.67 eV, which is lower than the surface band-gap energy (0.80 eV) at the $\bar{\Gamma}$ point by 0.13 eV. The E_b of 0.13 eV is again roughly 10 times larger than the energy of bulk excitons in Si.

Furthermore, the surface exciton on ZnO($10\bar{1}0$) surface has also been studied using TR-ARPES [24]. On the surface with hydrogen-induced work-function modifications under ultrahigh-vacuum conditions, a surface exciton is formed with

an ultrafast (200-fs) rate under band-gap excitation at 100 K. It has been concluded that the surface exciton is localized in the subsurface region and exhibits a very large E_b of 250 meV (E_b of bulk exciton in ZnO is 59 meV [10]). The electronic structure of the surface-exciton state has been interpreted in terms of bulk conduction band (CB) and valence band (VB), with a significant downward band bending near the surface, although the effects of reconstructions on surface-electronic structures have not been clarified.

The surface excitons on the reconstructed Si surfaces described above provide the best examples demonstrating the important role of reconstruction-induced surface electronic states on the formation of surface-specific excitonic states [18–23]. Additionally, as the semiconductor surfaces form quasi-2D systems, the intrinsic enhancement of the importance of Coulomb interactions, as well as the reduced screening, becomes important on the electron-hole correlation [25]. However, the effects originating from the quasi-2D character of the surfaces, which are inherently included in the properties of surface excitons, are less clear because of more drastic effects of the electronic-structure changes on the reconstructed Si surface. As the previous studies to capture the unambiguous correlation between the atomic and electronic properties of surfaces and the characteristic features of excitonic states formed on the surfaces are still limited, thorough understanding of how the semiconductor surfaces modify the characteristics of excitonic states remains elusive. Further studies for the surface excitons on semiconductor surfaces with different electronic and atomic structures are highly desirable. In this paper, we study the surface excitons on vacuum-cleaved InP(110)-(1 × 1) surface, which have different characteristics from those of other reconstructed semiconductor surfaces [1].

On the vacuum-cleaved (110) surface of InP, like other III-V semiconductors, no surface reconstructions are induced, but the surface atoms are relaxed normal to the surface from their positions in a bulklike layer within the first few layers from the surface, with keeping the dimensions of the unit cell unchanged [1]. Reflecting the characteristics of surface-atom relaxations, intrinsic surfaces states do not exist in the band-gap energy region; the surface-relaxation induced electronic states form mostly the surface-resonance states having high probability densities at the surface but energies within a projected bulk band, in particular near the $\bar{\Gamma}$ point [1,26–29]. Therefore, the highest-occupied and the lowest-unoccupied states, which play the important roles in exciton formation, are determined primarily by bulk states near the valence band maximum (VBM) and the conduction-band minimum (CBM). Furthermore, there are no surface band-bending effects on this surface, as the intrinsic surface states do not exist in the band-gap energy region [1]. These characteristics of electronic structures of InP(110)-(1 × 1) show significant differences from those of the surfaces on which surface excitons have been studied previously. The InP(110)-(1 × 1) surface provides an interesting and important system for which we study the surface-specific effects on the characteristics of surface excitons from a more general point of view.

In this paper, we study the surface excitons on InP(110)-(1 × 1) at 90 K, using TR-ARPES. Because of the intrinsic surface sensitivity of this technique, it is possible to observe the ultrafast relaxation of photoinjected electrons in the CB and the subsequent formation of an excitonic state near the surface on subpicosecond timescales. Furthermore, TR-ARPES has a unique capability to gain a deeper insight into the wave functions of excitons; angle-resolved photoemission spectroscopy directly measures the amplitudes of momentum- and energy-resolved Bloch functions of which the excitonic states are composed [30–32]. The method was applied, among others, to study the dynamics and electronic properties of excitons in organic and inorganic materials [15,22–24,33–40].

II. EXPERIMENTAL METHODS

Single crystals of Zn-doped InP with the hole concentration of 1.5×10^{17} cm^{-3} were grown via the vertical gradient freeze method (purchased from MTI). They were cleaved under ultrahigh-vacuum conditions ($<5 \times 10^{-11}$ Torr), and surface structures were characterized *in situ* using a scanning tunneling microscope. All samples showed well-ordered (1 × 1) surface structure, and concentrations of surface point defects were typically $<10^{-3}$ monolayer. A 76-MHz Ti-sapphire laser generated 75-fs laser pulses centered at photon energy of 1.70 eV. A portion of the fundamental output was converted to third-harmonic pulses for probing photoemission. The cross-correlation trace between pump and probe pulses in a β-barium borate crystal was well described by a Gaussian with a full width at half maximum of 110 ± 10 fs. The probe pulses passed a computer-controlled delay stage to set the time delay (Δt) with respect to the pump pulses, and pump and probe pulses were aligned coaxially and focused on the sample surfaces at 45° to surface normal. The pump-pulse fluence was set to give an excitation density ρ_0 of $1.0 \pm 0.1 \times 10^{17}$ cm^{-3}, which was evaluated using the formula: $\rho_0 = (F_p/h\nu_{\text{pump}})(1-R)\alpha$, with the fluence of pump pulse F_p, the reflectivity R, and the absorption coefficient α at excitation photon energy $h\nu_{\text{pump}}$. Probe-pulse fluences were less than 1/500 of those of pump pulses.

Using a hemispherical electron analyzer (SPECS, PHOIBOS 100) operated in an angle-resolved lens mode, equipped with a charge-coupled device detector, photoelectron images were recorded as a function of the photoelectron energy E_{mes} referenced to the work function of the analyzer and emission angle θ along the [001] crystal direction: surface-normal photoemission was along the [110] crystal direction. Under this geometry, the bulk Brillouin zone (BBZ) and the surface Brillouin zone (SBZ) have the relation shown in Fig. 1 [41,42]. As the emission angle θ corresponds to the parallel component of momentum ($k_{||}$) along the $\bar{\Gamma} - \bar{Y}$ ($= \bar{X}'$) direction of the SBZ, the measured photoemission image represents a one-dimensional cut, along $\bar{\Gamma} - \bar{Y}$ of the SBZ, of the two-dimensional projection of three-dimensional electron distributions. The measured photoemission images capture photoelectrons emitted from the initial states included in the projection plane (light-blue) in Fig. 1. The kinetic energy E_K of photoelectron and $k_{||}$ are two important quantities that characterize the photoemission. For determining E_K, we experimentally measured the low-energy cutoff energy E_{low} of the photoemission, which corresponded to the vacuum level of the sample [23], and determined E_K as $E_K = E_{mes} - E_{\text{low}}$.

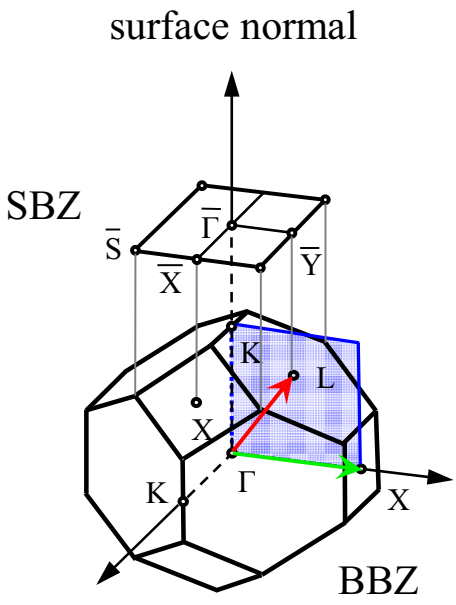

FIG. 1. Relation between the surface Brillouin zone (SBZ) and bulk Brillouin zone (BBZ) for InP with the (110) surface under the present experimental geometry. The plane (light blue) is the projection plane, and the red (green) arrow within the plane shows the direction from the Γ to *L* (Γ to *X)* points.

The $k_{||}$ was determined by the relation

$$k_{||} = \frac{1}{\hbar}\sqrt{2m_e E_K}\sin\theta, \tag{1}$$

with Planck's constant $\hbar$ and the electron rest mass m_e [41]. The measured images as a function of E_{mes} and θ were transformed to the images as a function of E_K and $k_{||}$, and then analyzed. In the measurements of photoemission images with an angle-resolved lens mode, the energy range of 1.00 eV and the emission angles ranging from -7.0° to $+7.0^\circ$ were captured simultaneously. The energy resolution was 40 meV and the angle resolution was $\pm 0.5^\circ$,

III. EXPERIMENTAL RESULTS

Figure 2(a) shows the momentum-integrated photoemission spectrum $I_{\langle k\rangle}(E_K, \Delta t)$ for $k_{||}$ ranging from 0 to 0.12 Å^{-1}, measured at $\Delta t = 20$ fs at 293 K under *s*-polarized 1.70-eV photoexcitation. It shows a broad peak at $E_K = 1.02$ eV. The electronic structures and the dynamics of energetic electrons in the CB are most conveniently characterized by the excess energy E_{ex} referenced to the CBM. The right-side scale, which is the same as the scale in Fig. 2(d), represents the energy of the initial state of photoemission in terms of E_{ex}, evaluated by the relation $E_{ex} = E_K + \chi - h\upsilon_{\text{probe}}$, where χ is the electron affinity and $h\upsilon_{\text{probe}}$ is the photon energy of probe light. The spectrum at $\Delta t = 20$ fs reflects a strong nonthermal feature of the nascent-electron distribution; the populations at high-energy states are significantly higher than at low-energy states [43]. Based on the theoretical band structure in Ref. [44], we can estimate the energies of the CB states reached by the optical transitions at the Σ region along the Γ-*K* direction from the heavy-hole (HH), light-hole (LH), and split-off (SO) valence band induced by the 1.70-eV pump light; it is 0.32, 0.26, and 0.11 eV from the CBM as indicated by arrows. The estimated energies can reasonably characterize the spectral features.

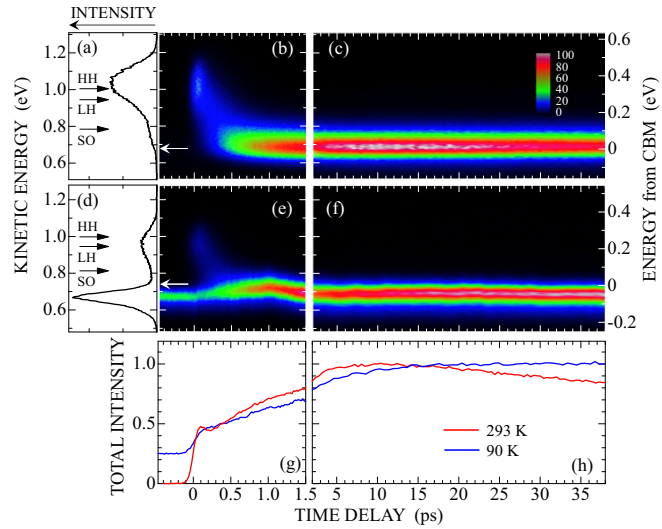

FIG. 2. (a) Momentum-integrated photoemission spectrum $I_{\langle k\rangle}(E_K, \Delta t)$ measured at $\Delta t = 20$ fs at 293 K under *s*-polarized 1.70-eV photoexcitation. (b) Temporal evolution of the $I_{\langle k\rangle}(E_K, \Delta t)$ at a short-time frame from -0.4 ps $< \Delta t < 1.5$ ps. The height of $I_{\langle k\rangle}(E_K, \Delta t)$, indicated by a color scale, is displayed as a function of Δt and E_K. (c) Temporal evolution of the $I_{\langle k\rangle}(E_K, \Delta t)$ at a long-time frame from 2 ps $< \Delta t <$ 38 ps. Right-side scale shows the initial-state energy referenced to the CBM. (d) Momentum-integrated photoemission spectrum $I_{\langle k\rangle}(E_K, \Delta t)$ measured at $\Delta t = 20$ fs at 90 K under *s*-polarized 1.70-eV photoexcitation. (e) Temporal evolution of the $I_{\langle k\rangle}(E_K, \Delta t)$ at 90 K at a short-time frame from -0.4 ps $< \Delta t <$ 1.5 ps. Height of $I_{\langle k\rangle}(E_K, \Delta t)$ is multiplied by a factor of 1.5 to show weak-intensity peaks clearer. (f) Temporal evolution of the $I_{\langle k\rangle}(E_K, \Delta t)$ at 90 K at a long-time frame from 2 ps $< \Delta t <$ 38 ps. Height of $I_{\langle k\rangle}(E_K, \Delta t)$ is displayed with the same scale as in (d). Right-side scale shows the initial-state energy referenced to the CBM. (g), (h) Temporal changes in the total intensity $I_T(\Delta t)$ induced by 1.70-eV photoexcitation at 293 K (red curve) and at 90 K (blue curve) in a (g) short-time frame, and (h) long-time frame. Arrows labeled heavy hole (HH), light hole (LH), and split off (SO) in (a) and (d) indicate the estimated energy levels of the conduction-band states reached by the optical transitions from the HH, LH, and SO valence band induced by the 1.70-eV pump light, based on the band calculation in Ref. [44]. The white arrows in (b) and (e) indicate the E_K of photoelectrons emitted from the CBM.

Figures 2(b) and 2(c) show the temporal evolution of $I_{\langle k\rangle}(E_K, \Delta t)$: a short-time frame from -0.4 to 1.5 ps in Fig. 2(b) and a long-time frame from 2 to 38 ps in Fig. 2(c). The intensity of $I_{\langle k\rangle}(E_K, \Delta t)$, indicated by a color scale, is displayed as a function of Δt and E_{ex} (right-side scale). The rapid relaxation occurs within 300 fs after excitation as shown in Fig. 2(b). The electron relaxation at $\Delta t <$ 1.5 ps at 293 K has been analyzed extensively in Ref. [43] to show that the quasithermalization in the electron subsystem is established at $\Delta t = 420$ fs, and then the cooling of hot electrons takes place in the hot-electron regime at

$\Delta t > 420$ fs. The red curve in Fig. 2(g) shows the energy- and momentum-integrated photoemission intensity [total intensity $I_T(\Delta t)$ hereafter] measured at Δt. It increases, after a rapid growth due to pump-induced injection of energetic electrons, to the maximum at $\Delta t = \sim 10$ ps, and then decreases at longer Δt. Because of the matrix-element effect and the k-dependent detection efficiency, $I_T(\Delta t)$ does not represent the electron density in the CB correctly, in particular during a short-time frame $\Delta t < 1$ ps [43]. However, at $\Delta t > 5$ ps, the spectroscopic features of photoemission do not depend on E_K and $k_{||}$; $I_T(\Delta t)$ gives a reasonable measure of electron density in the CB. The total intensity decays with a time constant of 200 ps at 293 K.

Figure 2(d) shows $I_{\langle k \rangle}(E_K, \Delta t)$ at $\Delta t = 20$ fs, and Figs. 2(e) and 2(f) display temporal evolutions of $I_{\langle k \rangle}(E_K, \Delta t)$ at short- and long-time frame at 90 K. One of the significant differences in spectral features from those at 293 K is that an intense photoemission peak is detected at the negative Δt region before the pump pulses excite samples. As any photoemission peaks cannot be detected without pump pulses, the photoemission at negative Δt (EX photoemission hereafter) can be ascribed to the state (EX state hereafter) that is generated by a pump pulse, and remains persistently in the time period of 13.2 ns until the next pump pulse excites the sample.

The blue curve in Fig. 2(g) shows $I_T(\Delta t)$ at 90 K. Starting from a finite value of 0.25, it gradually increases to the maximum value around $\Delta t = 10$ ps, and stays constant. It was not possible to determine the decay time of $I_T(\Delta t)$ at 90 K in the temporal regime available till 500 ps, at which $I_T(\Delta t)$ decreases only less than 10% of the maximum intensity. As the photoemission with essentially the same spectroscopic features is detected at negative time delays with the amount of 0.25 relative to the maximum intensity at $\Delta t \sim 10$ ps, we can estimate the decay time of EX state by assuming an exponential decay of the state; it is 9.5 ns, which is 50 times longer than the decay time of the electrons accumulated near the CBM at 293 K. The results in Fig. 2 show that the transient stabilities of long-lived states near the CBM are strongly temperature dependent, suggesting a possibility that the long-lived state formed at 90 K is not the same as that at 293 K.

At $\Delta t = 20$ fs, the excitation with 1.70-eV photons at 90 K injects energetic electrons at the CB states with $E_{ex} = 0.22$ eV, as seen in Fig. 2(d). As shown by arrows labeled HH, LH, and SO, the spectral features of the excitation-induced peaks are well explained by the transitions from HH, LH, and SO valence band to the CB by 1.70-eV photons. At the time frame with $\Delta t > 2$ ps, however, $I_{\langle k \rangle}(E_K, \Delta t)$ is dominated by one photoemission peak from EX state. Therefore, temporal changes in $I_{\langle k \rangle}(E_K, \Delta t)$ at the short-time frame from $\Delta t = 0$ to 1.5 ps shown in Fig. 2(e) reflect the relaxation of photoinjected energetic electrons in the Γ valley, governed by the Fröhlich mechanism of electron-phonon interaction [43], together with possible interactions with preexisting EX states. To clarify the relaxation process of energetic electrons at the short-time frame at 90 K, it is first necessary to identify the origin of EX state, and then to trace the dynamics of relaxations in energy- and momentum spaces. In this paper, we focus attention on the first issue of identifying EX state;

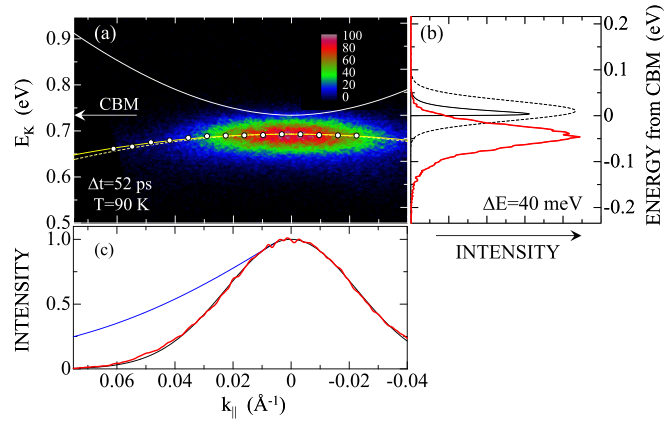

FIG. 3. (a) Photoemission image measured at $\Delta t = 52$ ps under excitation at 1.70-eV light pulses at 90 K. Intensities, specified by the color scale, are plotted as a function of $k_{||}$ and E_K (left-side scale). Estimated initial-state energy referenced to the CBM is indicated on the right-side scale. White dots in the figure display the peak-kinetic energies for the momentum-resolved photoemission spectra with a width of ± 0.0032 Å^{-1} . White curve shows the dispersion of the CB along the Γ-X direction. Solid (broken) yellow curve shows the dispersion of the HH valence band along the Γ-X (Γ-L) direction plotted as a function of $k_{||}$. They are shifted energetically to fit the result of $E_K^p(k_{||})$ at $k_{\|} = 0$. (b) Red curve shows the normal photoemission spectrum of the image shown in (a); photoemission intensities for $k_{\|} = 0 \pm 0.0032$ Å^{-1} are integrated. The solid black curve shows the Maxwell distribution function at 90 K, while the broken black curve shows the distribution function convolved with respect to the finite-energy resolution of 40 meV. (c) Momentum-resolved intensity of energy-integrated photoemission in the image shown in (a). Blue curve shows the calculated result of Eq. (6) for $a_B = 6$ Å. In the calculation, $\epsilon = 1 \times 10^{-4}$ radian was used. Black curve shows the Gaussian fitted to the results of $k_{\|}$-resolved intensity distribution (see the text).

the second issue is beyond the scope and to be published elsewhere.

To identify the origin of EX photoemission at 90 K, the spectroscopic features of the photoemission were studied in detail. Figure 3(a) shows the photoemission image measured at $\Delta t = 52$ ps. Photoemission intensities, specified by a color scale, are plotted as a function of $k_{||}$ and E_K (left-side scale). We emphasize the following four characteristic features of EX photoemission.

The first is the downward dispersion of EX photoemission. For making the dispersive feature of EX photoemission clearer, we determined the peak kinetic energy $E_K^p(k_{||})$ of the momentum-resolved spectrum at a given $k_{||}$ with a width of ± 0.0032 Å^{-1}. The determined peak kinetic energies are plotted by white dots as a function of $k_{||}$ in the figure. $E_K^p(k_{||})$ decreases with increasing $k_{||}$, showing a downward dispersion although the effect is small.

The second is that the kinetic energies of photoemission are substantially lower than those expected from the photoemission from the CBM. It was not possible to determine experimentally the kinetic energy E_K(CBM) of photoelectrons emitted from the CBM at 90 K, because of complicated spectral changes originating from the interaction between

preexisting EX state and the photoinjected electrons. However, we can estimate precisely the E_K(CBM) at 90 K, based on one important conclusion obtained in previous studies for the cleaved {110} surfaces of III-V compound semiconductors [1]. The ionization energy $\Phi_{\rm vac}$, defined as the energy distance from the VBM to the vacuum level, of InP(110)-(1 × 1) is independent of temperature; χ thus increases as E_G decreases as a function of temperature [1]. Based on the present experimental results at 293 K, we have determined that $\Phi_{\rm vac} = 5.74 \pm 0.02$ eV and $E_K(\text{CBM}) = 0.669$ eV for $h\upsilon_{\rm probe} = 5.07$ eV for the sample used in this paper. At 90 K, $E_G = 1.416$ eV, which is 0.065 eV wider than E_G (1.351 eV) at 293 K [45]. Therefore, E_K(CBM) is straightforwardly estimated to be 0.734 eV at 90 K for $h\upsilon_{\rm probe} = 5.07$ eV, which is indicated by the arrow labeled CBM in Fig. 3(a). The energy of EX state responsible for EX photoemission is evidently located below the CBM.

The third is the unique spectroscopic feature of EX photoemission. In Fig. 3(b), we show the surface-normal photoemission of the image in Fig. 3(a), obtained by integrating photoemission intensities for $k_\parallel = 0 \pm 0.0032$ Å^{-1}. The surface-normal photoemission spectrum shows an asymmetric line shape with a tail toward the *low-energy side*. In the same figure, we plotted the line shape of thermalized electron distribution near the CBM at 90 K by a solid black curve, and its spectrum convolved with respect to ΔE (= 40 meV) by the broken black curve. The convolved spectrum of photoemission from thermalized electrons near the CBM shows almost-symmetric line shape with a tail toward the *high-energy side*. The line shape of EX photoemission is qualitatively different from that expected for thermalized electrons neat the CBM.

The fourth is strongly $k_{||}$-dependent photoemission intensities. In Fig. 3(c), the $k_{||}$-resolved but energy-integrated intensity $I_{\langle E\rangle}(k_{||})$ is shown as a function of $k_{||}$. The intensity distribution is confined in the range of ± 0.07 Å^{-1}. The strongly $k_{||}$-dependent photoemission intensity, with the clear downward dispersion, excludes definitively the possibility that EX state is related to any localized electronic states associated with point defects in bulk and/or on the surfaces.

IV. DISCUSSION

Based on the experimental results described above, we can conclude that EX state is neither thermalized electrons at the bulk CBM nor localized electrons trapped at defect states in bulk and/or on the surface. The EX state is an intrinsic electronic state with the energy lower than the CBM by a few tens of millielectronvolts, and generates photoemissions in the localized momentum region including $\bar{\Gamma}$ of SBZ with a downward dispersion. In this section, we argue that EX state is the surface exciton formed on InP(110)-(1 × 1). We first examine critically the relation between the present results given in Sec. III and the theoretical consequences of exciton photoionization, which have been well documented in previous theoretical and experimental studies [15,22,30–32]. Then, we analyze the experimental results quantitatively to reveal characteristic features of EX excitonic state, which are significantly different from those of bulk excitons in InP. Finally, we discuss the physical factors which induce unique properties of the excitonic state on this surface.

A. TR-ARPES and the photoionization of excitons

In ARPES for electronic-structure determinations of solids, one tacitly assumes a definite initial one-electron energy level $E_I(\vec{\rm k})$ from which electrons are photoionized ($\vec{\rm k}$ being the wave vectors). In this independent quasiparticle picture (IQP) of photoemission for semiconductors, the kinetic energy $E_K(\vec{\rm k})$ of a photoelectron emitted from the level $E_I(\vec{\rm k})$ referenced to the VBM is given by

$$E_K(\vec{\rm k}) = h\upsilon_{\rm probe} + E_I(\vec{\rm k}) - \Phi_{\rm vac}. \tag{2}$$

The wave vector of photoelectron is linked to that of $E_I(\vec{\rm k})$ via the parallel-momentum conservation. Therefore, the initial-state energy $E_I(\vec{\rm k})$ and the wave vector can be obtained by measuring angle- and energy-resolved photoelectrons.

However, such an initial one-electron energy level is indefinite, in principle, for photoionization of excitons [30–32]. An exciton is a bound state between an electron and a hole only in their relative space, being a superposition of various electron-hole pair excitations with amplitude $f(\vec{k}_e, \vec{k}_h)$, where $\vec{k}_e$ and $\vec{k}_h$ are wave vectors of the electron and hole in IQP band structure [8–11]. In the Wannier model, applicable for most inorganic semiconductors, an excitonic state $|ex\rangle$ with its center-of-mass wave vector $\vec{K} = 0$ is defined as

$$|ex\rangle = \sum_{\vec{k}} f(\vec{k}, -\vec{k}) \hat{a}^+_{\vec{k}} \hat{b}^+_{-\vec{k}} |0\rangle, \tag{3}$$

where $\hat{a}^+_{\vec{k}}$ and $\hat{b}^+_{-\vec{k}}$ are creation operators of an electron with wave vector $\vec{k}$ and of a hole with wave vector $-\vec{k}$ in the IQP electronic structure, and $|0\rangle$ is the vacuum state.

In the photoionization processes of excitons, only electrons are emitted out of crystals, while the conjugate holes are left inside, and recoiled back to "original" valence-band states with the recoil energy $E_R(-\vec{k})$. Under momentum- and energy conservations, the photoemitted electron from an excitonic state has the momentum $\hbar\vec{\rm k}$ and the energy $E_K(\vec{k})$ given by

$$E_K(\vec{k}) = h\upsilon_{\rm probe} + E_{EX} - E_R(-\vec{k}) - \Phi_{\rm vac}, \tag{4}$$

where E_{EX} is the excitonic-state energy referenced to the VBM [31,32]. Therefore, the recoil of conjugates holes plays crucial roles in the photoionization of excitons; it governs the kinetic energy and momentum of photoemitted electrons. As $E_R(-\vec{k})$ is determined primarily by the dispersion of the valence state responsible for the excitonic state, the dispersion of $E_K(\vec{k})$ shows the dispersion same as that of the valence state.

On the other hand, the photoemission intensity, specified by $\hbar\vec{\rm k}$ and the energy $E_K(\vec{k})$, in the exciton photoionization is proportional to $|f(\vec{k}_e, \vec{k}_h)|^2$, such that angle-resolved photoemission spectroscopy directly measures the amplitudes of momentum- and energy-resolved IQP Bloch functions of which the excitonic states are composed. Therefore, TR-ARPES makes it possible, in principle, to determine

experimentally the correlation between an excitonic state and the IQP Bloch states responsible for the excitonic state.

B. EX photoemission and exciton photoionization

As described in Sec. II, the photoemission image measured under the present experimental geometry represents a one-dimensional cut, along the $\bar{\Gamma}-\bar{Y}$ of the SBZ, of the two-dimensional projection of three-dimensional electron distributions in the bulk electronic states. All states along the Γ-K([110]) direction in the BBZ are projected at the $\bar{\Gamma}$, contributing to surface-normal photoemission. Therefore, the normal photoemission gives the information exclusively for the states along the Γ-K direction, dispersive characteristics of which have been well studied theoretically. In the off-normal photoemission, however, the determination of $k_{||}$ fixes a point on the two-dimensional SBZ; the momentum $k_{\perp}$ normal to the surface can have a value anywhere along the rod extending into the three-dimensional BBZ [41]. Therefore, the off-normal photoemission at a given $k_{||}$ is a superposition of many contributions from such states that have different magnitudes of wave vectors depending on the directions in the BBZ in the projection plane; the dispersive characteristics of off-normal photoemission are complicated functions governed by the dispersions along many directions in the BBZ. Considering these features and limitations of the present photoemission results, we first discuss qualitatively the characteristic features of EX photoemission revealed in Fig. 3.

Despite the composite features in the off-normal emission mentioned above, it is clear in Fig. 3(a) that $E_K^p(k_{||})$ of EX photoemission decreases with increasing $k_{||}$, showing a clear downward dispersion. In view of the exciton-photoionization theory, the dispersion of $E_K^p(k_{||})$ results from the recoil of conjugates holes governed by the dispersion of the VB state responsible for the exciton state. As emphasized in Sec. I, the surface-relaxation induced electronic states on InP(110)-(1×1) surface form the surface-resonance states dipping into the bulk bands near the $\bar{\Gamma}$ point. Previous studies have shown that the minimum energy of the lowest-unoccupied surface-resonance state lies about 0.5 eV above the bulk CBM, while the highest-occupied surface-resonance state lies 0.4 eV below the bulk VBM [46,47]; the "surface band-gap energy" at the $\bar{\Gamma}$ is larger than the bulk band-gap energy by about 1 eV. In such energetic conditions, it is presumed that the electron-hole pair excitations responsible for the exciton are composed predominantly of the excitations in bulk states with lower energies, although the admixtures between bulk states and surface-derived states are significant at the surface region. Therefore, the bulk VB- and the CB-states are presumed to play important roles as the highest-occupied and the lowest-unoccupied states, which are crucial to characterize the excitonic structure at a given $k_{||}$ near the $\bar{\Gamma}$ point.

The solid (broken) yellow curve, pertaining to the results of $E_K^p(k_{||})$, is the dispersion of the bulk HH valence band along the Γ-X (Γ-L) direction as a function of $k_{||}$; the relation $k_{||}=k_X$ [$k_{||}=k_L\cos(54.7^{\circ})$] was used, where k_X (k_L) is the wave vector along the Γ-X (Γ-L) direction (see Fig 1). They are plotted with a vertical offset to fit the experimental result of $E_K^p(0)$ at $k_{\parallel}=0\,\text{Å}^{-1}$. The dispersion of $E_K^p(k_{||})$ is well described by the dispersion of HH band of bulk electronic structures. The reasonable agreement between the dispersion of $E_K^p(k_{||})$ and the dispersion of bulk-HH band supports our conclusion that EX photoemission is due to the photoionization of excitons. Furthermore, the agreement suggests strongly that the highest-occupied state responsible for the exciton is the bulk HH-valence band, which we assume in all the analyses described below.

As summarized in Sec. III, EX photoemission shows a unique asymmetric line shape with a tail toward the low-energy side. In view of Eq. (4) in the exciton-photoionization theory, the kinetic energy of photoelectrons is highest when $E_R(-\vec{k})=0$, and the energy decreases with increasing $E_R(-\vec{k})$ at larger magnitudes of $|\bar{k}|$. As the photoemission intensity, which is proportional to $|f(\vec{k},-\vec{k})|^2$, decreases with increasing $|\bar{k}|$ [31,32], the photoemission spectrum due to exciton photoionization is always associated with the low-energy tail, showing the asymmetry spectroscopic feature exactly the same as observed for EX photoemission.

As argued above, the qualitative features of EX photoemission are well described consistently and systematically by the theory of exciton photoionization. Therefore, we conclude that the EX photoemission is due to photoionization of the exciton formed on InP(110)-(1×1) at 90 K. We analyze below the spectral features of EX photoemission more quantitatively to reveal the characteristics of the excitonic state on this surface.

C. Spectral line-shape analysis of EX photoemission

Avoiding the complexity coming from composite features of off-normal emission mentioned in Sec. IV B, we first analyze the results of normal photoemission, which is contributed exclusively from the states along the Γ-K direction parallel to the surface-normal direction. In this case, the photoemission spectra including the recoil effects of holes can be analyzed using the result of HH dispersion along the Γ-K direction, $E_{HH}(k_K)$, where k_K is the wave vector along the Γ-K direction. The result of $E_{HH}(k_K)$ in the bulk band-structure calculations in Ref. [44] is shown in Fig. 4(a).

In Fig. 4(b), the normal photoemission spectrum at $\Delta t=52$ ps is displayed again by the green curve. To have deeper insight into the asymmetric spectral feature, the spectrum was deconvolved with respect to the finite-energy resolution ($\Delta E=40\,\text{meV}$) using the method described in Ref. [15], and the deconvolved amplitudes were plotted by open circles. The intensity increases abruptly at $E_K\approx0.71$ eV, and decreases with decreasing E_K. According to the exciton-photoionization theory, the recoil energy $E_R(k_K)$ is determined as $E_R(k_K)=E_{HH}(0)-E_{HH}(k_K)$ for a given wave vector k_K, and the kinetic energy $E_K(k_K)$ at k_K is evaluated by Eq. (4). To estimate the photoemission intensity $I_e(k_K)$ at k_K, we assume a hydrogen-like $1S$ state $\Psi_{1S}(r)$ for the exciton in a three-dimensional (3D) system. For $\Psi_{1S}(r)$, the modulus squared, $|\Phi_{1s}(k)|^2$, of the Fourier transform of $\Psi_{1S}(r)$ is given by [32,48,49]

$$|\Phi_{1s}(k)|^2=\frac{8(a_B)^3}{\pi^2\{1+k^2(a_B)^2\}^4}, \tag{5}$$

which corresponds to $|f(\vec{k}_e,\vec{k}_h)|^2$ in Eq. (3). In Eq. (5), a_B is the Bohr radius of the $1S$ exciton state and k is the wave

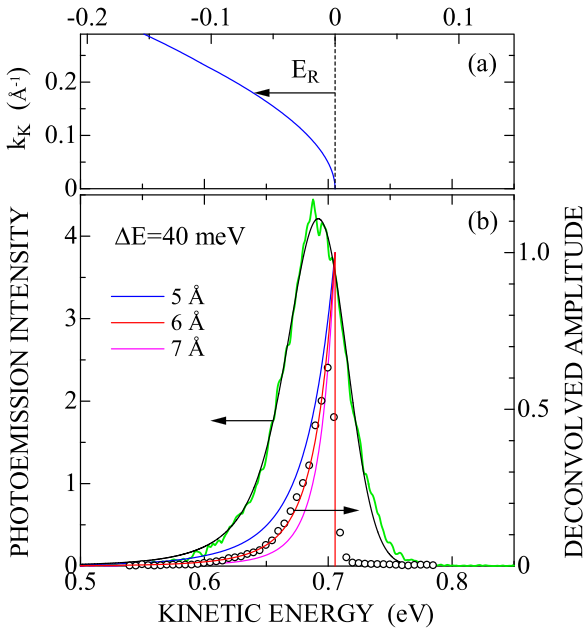

FIG. 4. (a) Dispersion of the bulk HH valence band along the Γ-K direction (from Ref. [44]). Energy at the Γ point is set to zero on the upper scale. (b) Green curve shows the normal photoemission spectrum in Fig. 3(a) obtained by integrating photoemission intensities for $k_{\|} = 0 \pm 0.0032$ Å^{-1}. Open circles are the photoemission intensities as a function of E_K obtained by deconvolving the normal-photoemission spectrum with respect to the finite-energy resolution of 40 meV. The blue, red, and purple curves show the calculated normal photoemission spectrum assuming the hydrogenlike 1S-state wave function with $a_B = 5$, 6, and 7 Å (for details see the text). The intensities are normalized with respect to the peak intensities (right-side scale) at $E_K = 0.706$ eV. Solid black curve displays the calculated normal photoemission spectrum with $a_B =$ 6 Å, convolved with respect to the energy resolution (40 meV) in the measurement. Peak kinetic energy (0.706 eV) of the calculated normal photoemission spectrum was adjusted in such a way that the convoluted spectrum gives the peak kinetic energy same as the experimental result.

vector from the Γ point along any directions in the BBZ. We discuss the limitations of assuming $\Psi_{1S}(r)$ for the excitonic states formed near the surfaces in the next section. However, it is expected that the radial probability density along the Γ-K direction (one-dimensional cut in the 3D distribution) can be estimated even though the exciton ground state will show deviations from $\Psi_{1S}(r)$ [49].

The blue, red, and purple curves in Fig. 4(b) show the theoretical spectra of $I_e(k_K)$ as a function of $E_K(k_K)$ for $a_B = 5$, 6, and 7 Å with $E_{EX} = 1.384$ eV (28 meV below the CBM), which corresponds to $E_K = 0.706$ eV. It is clear that the result for $a_B = 6$ Å describes reasonably well the kinetic-energy dependence of deconvolved photoemission intensity. In fact, the solid black curve, which shows the convolved calculated spectrum for $a_B = 6$ Å with respect to ΔE of 40 meV, reproduces well the experimental normal photoemission spectrum.

We then analyze the off-normal photoemission intensity, shown in Fig. 3(c), assuming the hydrogenlike 1S state $\Psi_{1S}(r)$ for the exciton. The off-normal photoemissions include the information, as an average, of the states along any direction to the point I from the Γ point in the BBZ, specified by the wave vector k_I with the angle θ_I from an infinitely small angle ϵ to $\pi/2$ with respect to the surface-normal direction; $k_{||} = k_I \sin\theta_I$ [41,42]. Because of the symmetry of $\Psi_{1S}(r)$, k_I along any directions satisfies Eq. (5). As Eq. (5) shows that the photoemission intensity is strongly reduced for larger magnitude of k_I, $I_{\langle E\rangle}(k_{||})$ at a given $k_{||}$ includes less contributions from states along the Γ to point I with small θ_I than those with θ_I close to $\pi/2$; $I_{\langle E\rangle}(k_{||})$ predominantly represents the radial probability density of EX state in the plane near parallel to the surface.

Using the relation $k_{||} = k_I \sin\theta_I$, the energy-integrated EX photoemission intensity $I_{\langle E\rangle}(k_{||})$ can be described as [15]

$$I_{\langle E\rangle}(k_{||}) = \int_{0+\epsilon}^{\pi/2} \frac{8(a_B)^3}{\pi^2[1 + \{k_{||}/\sin(\theta_I)\}^2 (a_B)^2]^4} d\theta_I. \quad (6)$$

The solid blue curve in Fig. 3(c) is the result of Eq. (6) obtained by numerical integration for $a_B = 6$ Å, which has been determined by the analysis of the radial probability density along the surface-normal direction. In contrast with the predicted result by Eq. (6), $I_{\langle E\rangle}(k_{||})$ is confined within the $k_{||}$ range much narrower than expected for the case of $a_B = 6$ Å. The result suggests that the radial spread in real space of EX state in the plane parallel to the surface is significantly wider than that along the surface-normal direction; the distribution of radial probability density of EX state is not spherical, but spheroidal.

The analytical expression of Fourier transform of the wave function of the lowest-state exciton having such a spheroidal distribution is not available; Eq. (5) is valid only for the spherical excitonic state in a 3D system. However, based on our finding that the radial probability density along the surface-normal direction is narrower than that in the plane parallel to the surface, we can estimate roughly the radial probability density in the planes parallel to the surface by assuming a purely 2D state of the exciton. For a 2D system, $k_{||}$ becomes a good quantum number characterizing the quantum states [40,41]; it represents wave vector within the 2D momentum plane. The $k_{||}$-resolved photoemission intensity $I_{\langle E\rangle}(k_{||})$ shown in Fig. 3(c) is well approximated by a Gaussian; $I_{\langle E\rangle}(k_{||}) = I_0 \exp(-a^2 k_{||}^2)$ with $a = 31$ Å, as shown by the black curve in Fig. 3(c). The $I_{\langle E\rangle}(k_{||})$ is proportional to the modulus squared, $|\Phi_{1S}^{2D}(k_{||})|^2$, of the Fourier transform of the lowest-state 2D exciton wave function $\Psi_{1S}^{2D}(x_{||})$. Therefore, from the inverse transformation of $\Phi_{1S}^{2D}(k_{||})$, $\Psi_{1S}^{2D}(x_{||})$ can be estimated; $\Psi_{1S}^{2D}(x_{||}) = N_{1S} \exp(-x_{||}^2/2\alpha^2)$ as a function of real-space coordinate $x_{||}$ in the 2D plane with the normalization constant N_{1S}. Therefore, it is estimated that the spatial spread in the plane parallel to the surface is characterized by the $x_{\|} =$ 44 Å, which gives $1/e$ of the maximum value of $|\Psi_{1S}^{2D}(x_{||})|$. The estimated spatial spread in the plane parallel to the surface is about seven times wider than that (6 Å) obtained along the surface-normal direction.

D. Characteristic features of the surface excitons on InP(110)-(1 × 1)

Quantitative analyses of the spectral line shape and $k_{||}$-dependent intensity of the photoemission from EX state have given that the exciton state is characterized by the binding

energy of 28 meV and by the anisotropic radial spread of 6 Å along the surface-normal direction and of 44 Å in the plane parallel to the surface. These excitonic properties are significantly different from those of the exciton in bulk InP, which is characterized by $E_b = 5.2$ meV and the spherical radial spread with $a_B = 113$ Å [10]. Therefore, the EX state is the excitonic state specific to the InP(110)-(1 × 1) surface, i.e., the surface exciton. Below we discuss possible mechanisms that give the significant differences in excitonic properties on this surface.

Previous theoretical studies for the vacuum-cleaved InP(110) surface show that the atomic displacements associated with the surface relaxation are converged within the first four layers from the surface, within 6 Å from the topmost layer (the distance between {110} planes in InP is 2.0 Å) [27–29]. Many physical properties in the surface layers with the relaxed atomic configurations differ from those in the bulk InP with the amounts dependent on the distance z from the surface. In the following arguments, however, we assume that the surface layers form a quasi-2D *surface region* with a depth δ, characterized by uniform surface-specific materials constants within the region, neglecting their depth dependences for simplicity.

In the theory of excitons based on the Wannier equation [9,10], E_b and a_B for the lowest state of exciton in a 3D system is given by $E_b = 13.6(\mu/m_e)\varepsilon^{-2}$ [eV] and $a_B = 0.529(m_e/\mu)\varepsilon$ [Å], where μ is the reduced mass of the exciton. Both quantities are dependent on zero-frequency dielectric constant ε in a system; $\varepsilon = 12.6\varepsilon_0$ in bulk InP (ε_0 being the permittivity of free space) [50]. However, in the surface region, the dielectric constant changes to the surface dielectric constant $\varepsilon_{\rm surf}$ by the reduced screening. On the topmost surface layer (z = 0), $\varepsilon_{\rm surf}(0) = (\varepsilon + \varepsilon_0)/2 = 6.8\varepsilon_0$, being the average of the two media separated by the interface between the semiconductor and vacuum [51]. Therefore, the $\varepsilon_{\rm surf}$, which governs primarily the excitonic properties, can have the magnitude $6.8\varepsilon_0 < \varepsilon_{\rm surf} < 12.6\varepsilon_0$, smaller than the bulk value of ε. Therefore, a larger value of E_b of the exciton in the surface region is presumed; for $\varepsilon_{\rm surf}(0)$, $E_b = 18$ meV, which is 3.4 times larger than the bulk value.

When the excitonic state with larger binding energy can be formed on the surface region, it is presumed that the state is confined only in the surface region and forms a 2D excitonic state. In Sec. VI C, we have determined the $a_B = 6$ Å along the surface-normal Γ-K direction assuming a hydrogenlike 1S state for the exciton. In view of the anisotropic radial probability densities of EX state and of the depth-dependent $\varepsilon_{\rm surf}$ mentioned above, a hydrogenlike 1S state with 3D distributions is not an appropriate approximation. Then, we reinterpret that the estimated magnitude of $a_B = 6$ Å is a measure of the depth of the surface layer δ within which the surface excitons are confined. With this confinement in the surface region, the radial spread in real space along the direction parallel to the surface is characterized by the magnitude of 44 Å.

It is well known that in the system characterized by the same set of material constants, the 2D exciton has 4× larger E_b and a half of a_B, compared with those of the 3D exciton [9]. Therefore, for such a 2D-excitonic state confined in the surface region with $\varepsilon_{\rm surf}$, $E_b = 54.4(\mu/m_e)\varepsilon_{\rm surf}^{-2}$ [eV] and $a_B = 0.265(m_e/\mu)\varepsilon_{\rm surf}$ [Å]. When we assume $\varepsilon_{\rm surf} = 10.3\varepsilon_0$, then $E_b = 30$ meV and $a_B = 46$ Å, both of which agree reasonably well with the experimental results of the surface exciton on InP(110)-(1 × 1). Therefore, we conclude that the surface exciton on InP(110)-(1 × 1) is characterized by the spheroidal radial probability density specified by the radial spread of ∼44 Å in the plane parallel to the surface, and confined within the surface-layer depth of ∼6 Å. As argued above, the reduced screening and two-dimensional confinement in the surface region play crucial roles to govern the excitonic properties on InP(110)-(1 × 1).

In the discussions described above, we have assumed that the surface exciton is composed of the bulk HH valence-band states and the bulk CB states near the Γ. The assumption is based on the fact that the minimum energy of the lowest-unoccupied surface-resonance state lies about 0.5 eV above the bulk CBM, while the highest-occupied surface-resonance state lies 0.4 eV below the bulk VBM at the $\bar{\Gamma}$ [46,47]. However, in view of the quasi-2D characters of the surface excitons confined within the surface region, more precise evaluation of possible roles of the surface-resonance states is an important issue to have deeper insight into the exciton wave functions on InP(110) surfaces. The clarification of anisotropy of exciton wave function within the planes parallel to the surface may provide a clue to judge the role of surface-resonance states. Reflecting the structural anisotropy of InP(110) surface, the dispersive characteristics of the occupied and unoccupied surface-resonance states along different directions in the SBZ are different [1,46,47]. When the surface-resonance states are significantly involved in the wave function of the surface exciton, the dispersive features of photoemission signals of exciton photoionization may potentially be different, depending on the direction in the SBZ. In this paper, we measured the dispersion characteristics of photoemission signals of the surface-exciton photoionization only along the $\bar{\Gamma} - \bar{Y}$ ($= \bar{X}'$) direction of the SBZ; the dispersive features along other different directions could not be measured for the same sample because of some limitations of our experimental apparatus. We leave the elucidation of possible anisotropy of exciton wave function within the planes parallel to the surface open as an interesting and important future study.

The surface exciton on InP(110)-(1 × 1), which is formed as an intrinsic electronically excited state with the lowest energy by the relaxation of high-energy electron-hole pair states, shows the long lifetime of 9.5 ns at 90 K. This feature of the stability is like the surface excitons formed on the reconstructed Si(100)-c(2 × 1) [22,23] and on ZnO(10$\bar{1}$0) [24] under the ultrahigh-vacuum conditions. As shown in Fig. 2, the surface exciton is formed after a finite time delay of ∼2 ps under band-gap excitation. The formation time includes several processes: the energy relaxation of photoinjected electron-hole pairs in the CB and VB bands under the presence of surface excitons, and the electron-hole correlation to form the excitonic states at the surface region. The dynamics of the relaxation from the high-energy electron-hole pair states to the surface-exciton state will be studied in a separate paper.

V. SUMMARY

Using TR-ARPES, we have studied the characteristics of the long-lived EX photoemission peak emitted from

InP(110)-(1 × 1) surface at 90 K. EX photoemission shows the following features: (i) the energy of EX state lower than the CBM of bulk electronic state with respect to the VBM, (ii) the downward dispersion with strongly k-dependent intensities, and (iii) unique spectral line shape with tails extending toward low-energy side. We have identified the initial state of EX photoemission to be the surface exciton specific to InP(110)-(1 × 1) surface, since the unique features of EX photoemission mentioned above are well described systematically in terms of the exciton-photoionization theory. Based on the quantitative analyses in terms of exciton-photoionization theory, we have shown that the radial probability density of the exciton is spheroidal, confined within ∼ 6 Å from the surface along the surface-normal direction and spread in the range of ∼ 44 Å in the plane parallel to the surface, being a quasi–two-dimensional excitonic state. The binding energy of 28 meV and the radial spread of ∼ 44 Å are consistent with the exciton theory based on the Wannier equation when the dielectric constant in the surface region is assumed to be $10.3\varepsilon_0$, which is in the reasonable range predicted from the dielectric constants of bulk InP and of the topmost surface layer. In view of the fact that the surface-specific electronic states induced by surface relaxation on this surface form surface resonance states, we have pointed out the important roles of both reduced screening effects and the two-dimensional confinement at the surface region on the characteristics of the surface exciton on InP(110)-(1 × 1). Based on these several important findings presented in this paper, more extensive studies for different semiconductor surfaces using TR-ARPES with higher energy resolution, together with advanced theoretical studies, are needed to allow for a full characterization of surface excitons on semiconductor surfaces in general.

ACKNOWLEDGMENT

This paper was supported by Japan Society for the Promotion of Science KAKENHI Grants No. 24000006 and No. 19H01826.

[1] W. Mönch, *Semiconductor Surfaces and Interfaces* (Springer, Berlin, 1995).
[2] K. Oura, V. G. Lifshits, A. A. Saranin, A. V. Zotov, and M. Katayama, *Surface Science: An Introduction* (Springer, Berlin, 2003).
[3] T. Fauster, L. Hammer, K. Heinz, and M. A. Schneider, *Surface Physics: Fundamentals and Methods* (Walter de Gruyter GmbH, Berlin, 2020).
[4] L. Reggiani, *Hot Electron Transport in Semiconductors* (Springer, New York, 1985).
[5] R. Haight, Surf. Sci. Rep. **21**, 275 (1995).
[6] C. Delerue and M. Lannoo, *Nanostructures: Theory and Modeling, Nanoscience and Technology* (Springer Verlag, Berlin, 2004).
[7] A. Polman and H. A. Atwater, Nat. Mater. **11**, 174 (2012).
[8] R. J. Elliott, Phys. Rev. **108**, 1384 (1957).
[9] H. Haug and S. W. Koch, *Quantum Theory of the Optical and Electronic Properties of Semiconductors* (World Scientific, Singapore, 1990).
[10] P. Y. Yu and M. Cardona, *Fundamentals of Semiconductors: Physics and Materials Properties* (Springer, Berlin, 1996).
[11] Y. Toyozawa, *Optical Processes in Solids* (Cambridge University Press, New York, 2003).
[12] S. W. Koch, G. Khitrova M.Kira, and H. M. Gibbs, Nat. Mater. **5**, 523 (2006).
[13] R. A. Kaindl, M. A. Carnahan, D. Hägele, R. Lövenich, and D. S. Chemla, Nature (London) **423**, 734 (2003).
[14] P. Steinleitner, P. Merkl, P. Nagler, J. Mornhinweg, C. Schüller, T. Korn, A. Chernikov, and R. Huber, Nano Lett. **17**, 1455 (2017).
[15] H. Tanimura, K. Tanimura, and P. H. M. van Loosdrecht, Phys. Rev. B **100**, 115204 (2019).
[16] K. C. Pandey, Phys. Rev. Lett. **47**, 1913 (1981); **49**, 223 (1982).
[17] F. Ancilotto, W. Andreoni, A. Selloni, R. Car, and M. Parrinello, Phys. Rev. Lett. **65**, 3148 (1990).
[18] M. Rohlfing and S. G. Louie, Phys. Rev. Lett. **83**, 856 (1999).
[19] M. Rohlfing and J. Pollmann, Phys. Rev. Lett. **88**, 176801 (2002).
[20] P. Chiaradia, A. Cricenti, S. Selci, and G. Chiarotti, Phys. Rev. Lett. **52**, 1145 (1984).
[21] F. Ciccacci, S. Selci, G. Chiarotti, and P. Chiaradia, Phys. Rev. Lett. **56**, 2411 (1986).
[22] M. Weinelt, M. Kutschera, T. Fauster, and M. Rohlfing, Phys. Rev. Lett. **92**, 126801 (2004).
[23] M. Weinelt, M. Kutschera, R. Schmidt, C. Orth, T. Fauster, and M. Rohlfing, Appl. Phys. A **80**, 995 (2005).
[24] J.-C. Deinert, D. Wegkamp, M. Meyer, C. Richter, M. Wolf, and J. Stähler, Phys. Rev. Lett. **113**, 057602 (2014).
[25] K. F. Mak, J. Shan, and T. F. Heinz, Phys. Rev. Lett. **106**, 046401 (2011).
[26] X. Zhu, S. B. Zhang, S. G. Louie, and M. L. Cohen, Phys. Rev. Lett. **63**, 2112 (1989).
[27] J. L. A. Alves, J. Hebenstreit, and M. Scheffler, Phys. Rev. B **44**, 6188 (1991).
[28] B. Engels, P. Richard, K. Schroeder, S. Blügel, Ph. Ebert, and K. Urban, Phys. Rev. B **58**, 7799 (1998).
[29] Ph. Ebert, Surf. Sci. Rep. **33**, 121 (1999).
[30] E. Perfetto, D. Sangalli, A. Marini, and G. Stefanucci, Phys. Rev. B **94**, 245303 (2016).
[31] H. Ohnishi, N. Tomita, and K. Nasu, Int. J. Mod. Phys. B **32**, 1850094 (2018).
[32] A. Rustagi and A. F. Kemper, Phys. Rev. B **97**, 235310 (2018).
[33] E. Varene, L. Bogner, C. Bronner, and P. Tegeder, Phys. Rev. Lett. **109**, 207601 (2012).
[34] X. Cui1, C. Wang1, A. Argondizzo, S. Garrett-Roe, B. Gumhalter, and H. Petek, Nat. Phys. **10**, 505 (2014).
[35] X.-Y. Zhu, J. Electron Spectrosc. Relat. Phenom. **204**, 75 (2015).
[36] H. Tanimura and K. Tanimura, Phys. Rev. B **102**, 045204 (2020).
[37] H. Tanimura and K. Tanimura, Phys. Rev. B **102**, 235202 (2020).

[38] J. Madeo, M. K. L. Man, C. Sahoo, M. Campbell, V. Pareek, E. L. Wong, A. Al-Mahboob, N. S. Chan, A. Karmakar, B. M. K. Mariserla, X. Li, T. F. Heinz, T. Cao, and K. M. Dani, Science **370**, 1199 (2020).

[39] R. Wallauer, R. Perea-Causin, L. Münster, S. Zajusch, S. Brem, J. Güdde, K. Tanimura, K.-Q. Lin, R. Huber, E. Malic, and U. Höfer, Nano Lett. **21**, 5867 (2021).

[40] M. K. L. Man, J. Madéo, C. Sahoo, K. Xie, M. Campbell, V. Pareek, A. Karmakar, E. L. Wong, A. Al-Mahboob, N. S. Chan, D. R. Bacon, X. Zhu, M. M. M. Abdelrasoul, X. Li, T. F. Heinz, F. H. da Jornada, T. Cao, and K. M. Dani1, Sci. Adv. **7**, eabg0192 (2021).

[41] E. W. Plummer and W. Eberhardt, in *Advances in Chemical Physics*, edited by I. Prigogine and S. A. Rice (Wiley, New York, 1982), Vol. 49, pp. 533–656.

[42] J. Kanasaki, H. Tanimura, and K. Tanimura, Phys. Rev. Lett. **113**, 237401 (2014).

[43] K. Tanimura, H. Tanimura, and J. Kanasaki, Phys. Rev. B **106**, 125204 (2022).

[44] Y.-S. Kim, M. Marsman, G. Kresse, F. Tran, and P. Blaha, Phys. Rev. B **82**, 205212 (2010).

[45] I. Vurgaftman, J. R. Meyer, and L. R. Ram-Mohan, J. Appl. Phys. **89**, 5815 (2001).

[46] R. P. Beres, R. E. Allen, and J. D. Dow, Phys. Rev. B **26**, 5702 (1982).

[47] L. Sorba, V. Hinkel, H. U. Middelmann, and K. Horn, Phys. Rev. B **36**, 8075 (1987).

[48] G. M. Kavoulakis, Y.-C. Chang, and G. Baym, Phys. Rev. B **55**, 7593 (1997).

[49] . F. Schweiner, J. Main, and G. Wunner, and C. Uihlein, Phys. Rev. B **95**, 195201 (2017).

[50] M. Hass and B. W. Henvis, J. Phys. Chem Solids **23**, 1099 (1962).

[51] A. Laubsch, K. Urban, and Ph. Ebert, Phys. Rev. B **80**, 245314 (2009).